Bulletin of the Seismological Society of America, Vol 72, No 2, pp 571-596, April 1982

STRONG-MOTION MODELING OF THE IMPERIAL VALLEY EARTHQUAKE OF 1979

By Stephen Hartzell* and Donald V. Helmberger

ABSTRACT

Twelve three-component strong-motion displacement records are modeled for the 1979 Imperial Valley earthquake to recover the distribution of slip on the Imperial fault plane. The final model, for which point source responses are calculated by a discrete wavenumber/finite element technique, uses a structure with gradients in material properties rather than layers. The effects of a velocity gradient are investigated by comparing synthetics with a layer-over-a-half-space model using generalized rays. It is shown that a uniform fault rupture model on a rectangular fault plane does not explain the data. The preferred fault model has slip concentrated below 5 km (in the basement material) and between the epicenter (5 km south of the international border) and Highway 80. Within this region, there appears to be two localized areas of larger dislocations; one just north of the border near Bonds Corner and a second under Interstate 8 at Meloland Overpass. A major arrival associated with large amplitude vertical accelerations (up to 1.7 *g*) is identified in the El Centro array records. This arrival has an *S-P* time of approximately 2.3 sec at many of the array stations and is modeled as originating from a localized source 8 km to the south of the array. The moment is estimated to be 5.0 × 10^{25} dyne-cm from the strong-motion records, which is consistent with teleseismic body-wave estimates. The preferred fault model is strike-slip with a 90° dip. The average strike is 143°. However to explain vertical waveforms near the fault trace, a corrugated or wiggly fault plane is introduced. The average rupture velocity is in the range 2.5 to 2.7 km-sec (0.8 to 0.9 times the basement shear-wave velocity). The preferred model has unilateral rupture propagation to the north, although the data would allow a small amount of propagation to the south. The estimated stress drop for the entire fault plane is only 5 to 10 bars; however, the stress drop over the more localized sources is about 200 bars. The fault model is consistent with the pattern of seismicity and observations of aseismic creep in the Imperial Valley and suggests that the southern half of the Imperial fault acts as a locked section which breaks periodically.

Introduction

This paper presents results on the modeling of strong ground motion displacement records for 12 of the near-source stations for the 15 October 1979 Imperial Valley earthquake (M_L = 6.6). The main objective of the work reported on here is to determine the general distribution of slip which occurred on the Imperial fault during the 15 October earthquake. Generalized ray theory with the Cagniard-de Hoop technique is used to calculate displacements for point shear dislocations for a layer-over-a-half-space model. These results are compared with displacements calculated using a discrete wavenumber/finite element approach for a vertical velocity gradient model. With both techniques, the point shear dislocation responses are summed to form a finite fault. We are primarily concerned with modeling the near-source displacements. However, our analysis also offers some constraints on the possible origin of the unusual high-amplitude accelerations recorded near the

* Present address U S Geological Survey, MS-77, 345 Middlefield Road, Menlo Park, California 94025

Imperial fault. The measured surface offsets and the distribution of aftershocks are also considered and discussed in terms of the preferred fault model.

The origin time of the 1979 Imperial Valley earthquake is 23hr16min54.5sec with an epicenter of 32.63°N, 115.33°W, or approximately 5 km south of the international border (Brady *et al.*, 1980). The estimated focal depth is 12 km. However, the above values are sensitive to the choice of velocity structure and the distribution of stations. Archuleta and Spudich (1981) have obtained the following estimates: origin time 23hr16min54.4sec, epicenter 32.66°N, 115.33°W, depth 8.0 km. The surface-wave moment is estimated to be 6.0×10^{25} dyne-cm from long-period Love and Rayleigh waves at Berkeley and Pasadena, and 7.0×10^{25} dyne-cm from an average of seven IDA station Rayleigh waves at 200 to 250 sec (Kanamori and Regan, 1981). The 1979 Imperial Valley earthquake is not particularly large compared to other recent southern California events: the 1968 Borrego Mountain earthquake, M_0 =

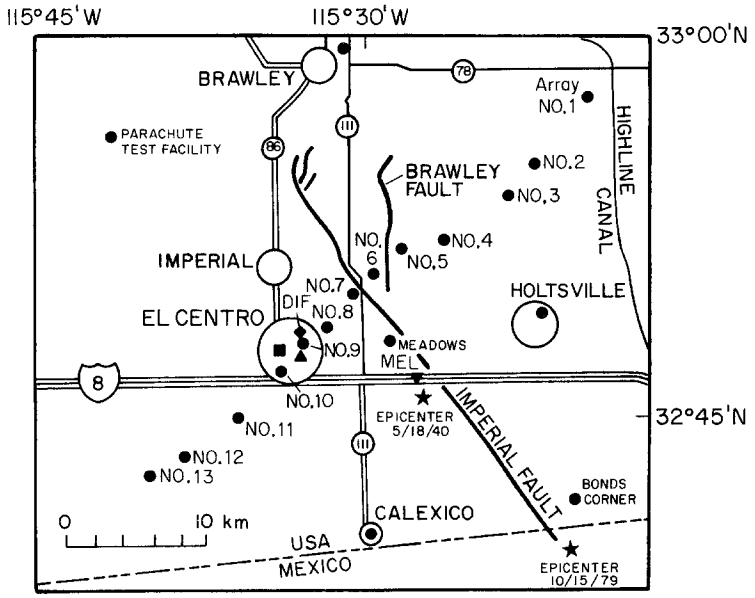

FIG. 1. Area map of the southern Imperial Valley showing the surface traces of the Imperial and Brawley faults and the locations of strong-motion instruments. The El Centro array is numbered 1 through 13.

11.2×10^{25} dyne-cm (Burdick and Mellman, 1976), and the 1971 San Fernando earthquake, $M_0 = 8.6 \times 10^{25}$ dyne-cm (Langston, 1978). However, it is a very significant event because of the rich set of strong-motion accelerograms recorded at close distances, and the largest peak accelerations recorded to date of 1.7 *g*.

The remainder of this paper is divided into four sections. The first section contains a qualitative investigation of the amplitude distribution and relative patterns of the strong-motion data as a prelude to quantitiative calculations. The second section discusses the finite-fault modeling technique. The third section presents and discusses several models of faulting. Here, we make use of the qualitative observations made in the first section. In the final section, the preferred fault model is discussed in terms of the faulting patterns and the apparent mode of strain release in the Imperial Valley.

Qualitative Investigation of the Strong-Motion Data

Before becoming involved in the specifics of deterministic finite-fault models, we first look at the strong-motion data set in an over-all, qualitative manner. When using involved, finite-fault computer codes, it is possible to convince oneself incorrectly that certain fault parameters are well constrained, simply because a match is made between synthetic ground motion and the observations. This pitfall exists

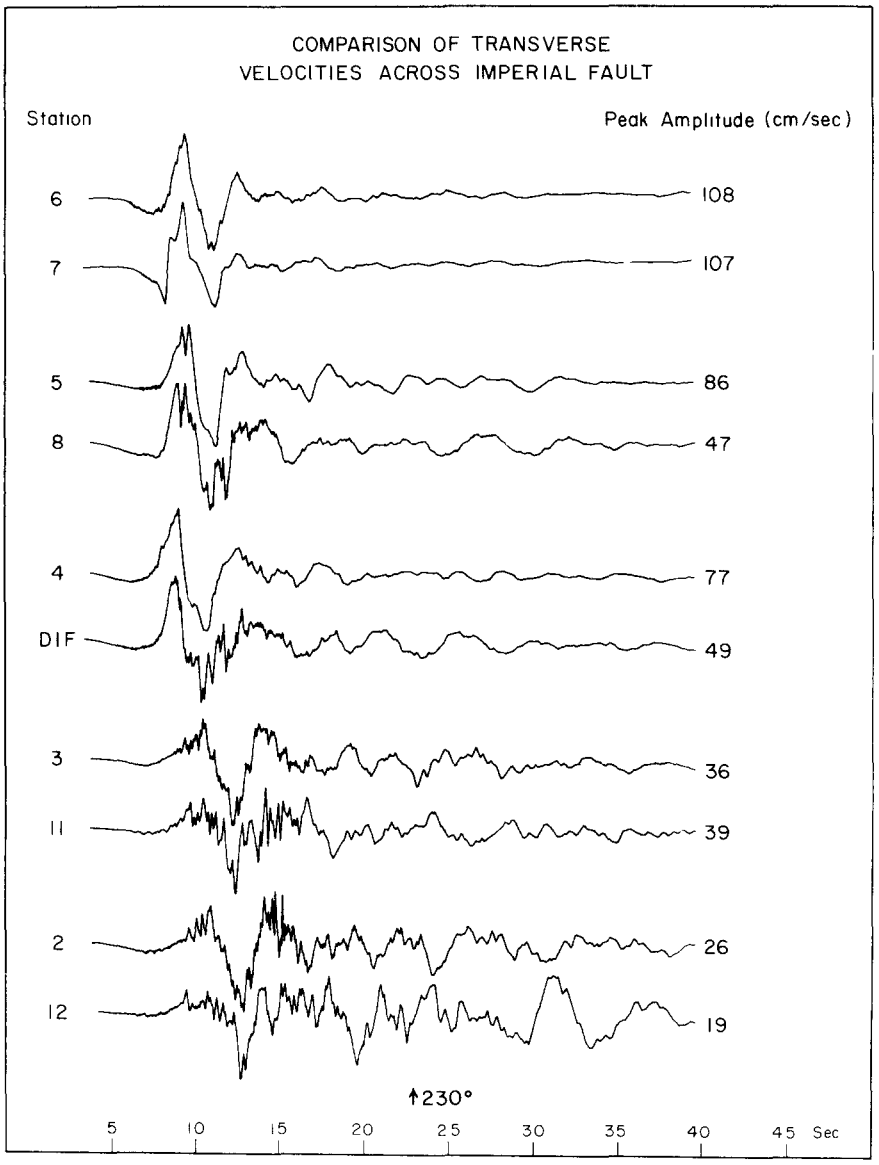

FIG. 2. Comparison of transverse (*SH*) velocities from the El Centro array for pairs of stations on either side of the Imperial fault and approximately the same distance from the fault trace.

because of the nonuniqueness of the solution and is also true if one relies on a poorly constrained inversion. Therefore, we wish to first gather as much insight from the data as possible before attempting to model it.

Figure 1 is a map of the southern Imperial Valley showing the surface traces of

the Imperial and Brawley faults and the locations of strong-motion instruments of interest here. Additional records obtained at stations further to the north and south (not in Figure 1) are much lower in amplitude. Stations numbered 1 through 13 comprise the El Centro strong-motion array and will be referred to as the array stations. Epicenters for both the 1979 and 1940 Imperial Valley earthquakes are indicated by stars. Similarities and differences between these two events will be discussed in the final section.

During the 1979 earthquake, ground breakage occurred on both the Imperial and Brawley faults. Surface faulting on the Imperial fault is primarily right lateral with maximum offsets of 60 to 70 cm on the section of the fault extending 5 to 10 km north of the border (Sharp *et al.*, 1981). As one moves further north, the magnitude of the surface offsets decreases. Near the northern end of the Imperial fault at Harris Road on the periphery of Mesquite Lake, surface faulting is primarily normal with the east side down. There are no surface offsets in the epicentral region or

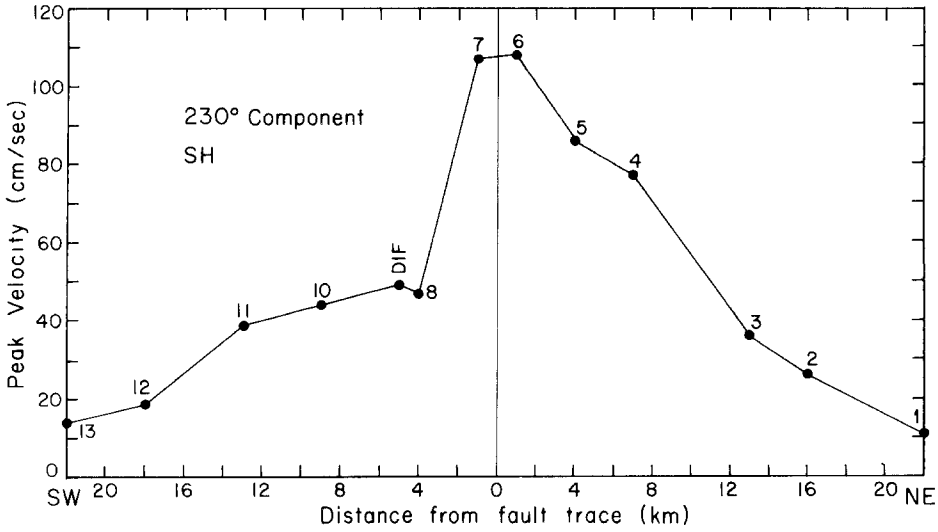

FIG. 3. Peak transverse (*SH*) velocities for the El Centro array plotted as a function of distance from the closest point on the Imperial fault.

within 5 km of the international border. Offsets on the Brawley fault are mainly normal with the west side down and secondary in amplitude to those on the Imperial fault.

Figure 2 compares horizontal velocities from the 230° components of the array stations. Five pairs of records are shown, each comparing stations laying on opposite sides of the Imperial fault, and at approximately the same distance from the fault (Figure 1). The 230° component is approximately transverse to the Inperial fault. For strike-slip motion on the Imperial fault, tne 230° component is dominated by *SH* motion. There is a high degree of correlation between waveforms in Figure 2 and thus symmetry in the *SH* radiation across the Imperial fault. Two inferences can be made from this observation. First, slip on the Brawley fault cannot be an important factor in the observed strong ground motion. If the contribution from the Brawley fault were significant, the above symmetry would not exist. We do not consider further here, motion on the Brawley fault, other than to speculate in the final section that it might be sympathetic or induced slip. Second, since a maximum

in the *SH* radiation pattern lies along the fault strike for a strike-slip mechanism, the 230° component "sees" the entire fault plane of the Imperial fault. Unlike the vertical and radial components, the 230° component is not strongly sensitive, except for a distance effect, to any particular segment of the fault plane. Then, given the simplicity and uniformity of the *SH* waveforms, their general shape can be explained by a simple Haskell fault model. However, the good symmetry in the *SH* waveforms on the 230° component is not carried over to the *P-SV* waveforms on the 140° vertical components. Thus, there are added complexities not explained by a Haskell model.

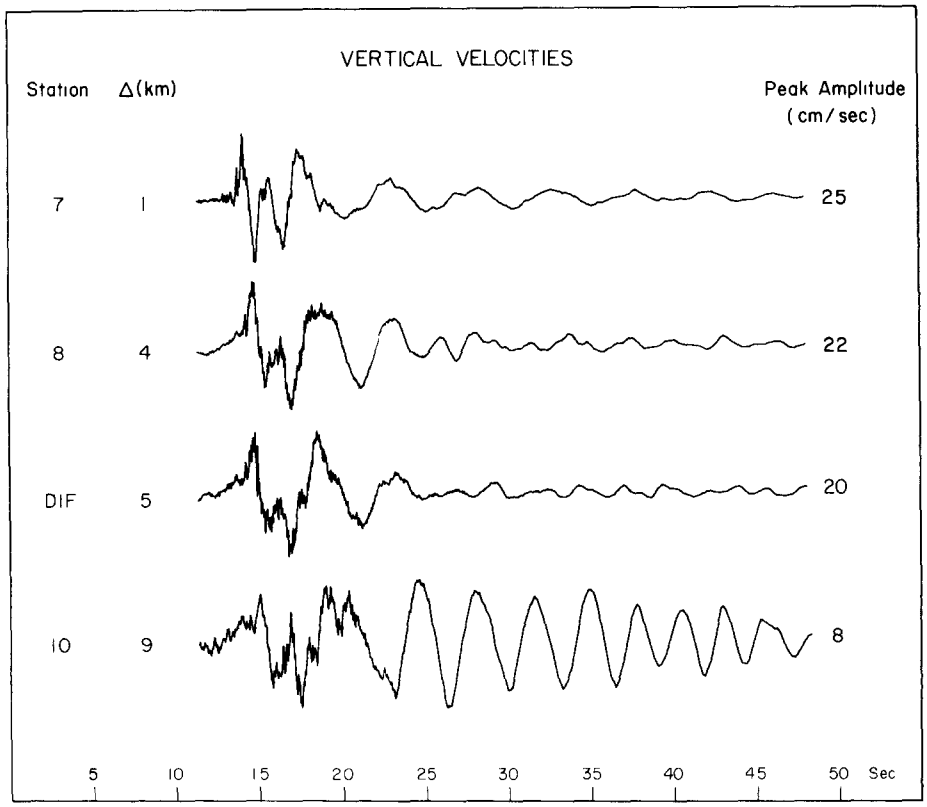

FIG. 4. Vertical velocities from the El Centro array plotted as a function of distance from the Imperial fault.

Futher insight into the faulting complexities can be obtained by considering the peak amplitudes. Peak *SH* velocities are plotted in Figure 3 for the array stations as a function of distance from the Imperial fault. There is asymmetry in the *SH* amplitude pattern. Amplitudes on the NE side of the fault are significantly higher than those on the SW side. For a strike-slip fault with a strike equal to the average trend of the surface trace of the Imperial fault (N143°E), the pattern in Figure 3 should be symmetric about zero. [We assume here that the fault dip is not significantly different from 90°. Analysis of teleseismic records indicates that a dip less than 75° is unlikely (Gordon Stewart, personal communication, 1981).] It is possible to explain the asymmetric *SH* pattern by a different strike on part or parts of the Imperial fault at depth. Of course, there are alternative explanations. Local amplification due to lateral heterogeneity may be a factor. However, *P*-wave

amplitudes offer some supportive evidence for the varying strike hypothesis. *P*-wave radiation should be nearly nodal along the strike of the Imperial fault (array stations 6 and 7) for a predominantly strike-slip mechanism. But, *P*-wave amplitudes on the vertical component are maximum near the strike of the fault (see Figure 4). A simple fault plane with a constant strike and a strike-slip mechanism cannot explain these data.

An indication of the depth of faulting is possible from a cursory investigation of the vertical strong motion. In Figure 4, vertical velocity records are plotted as a

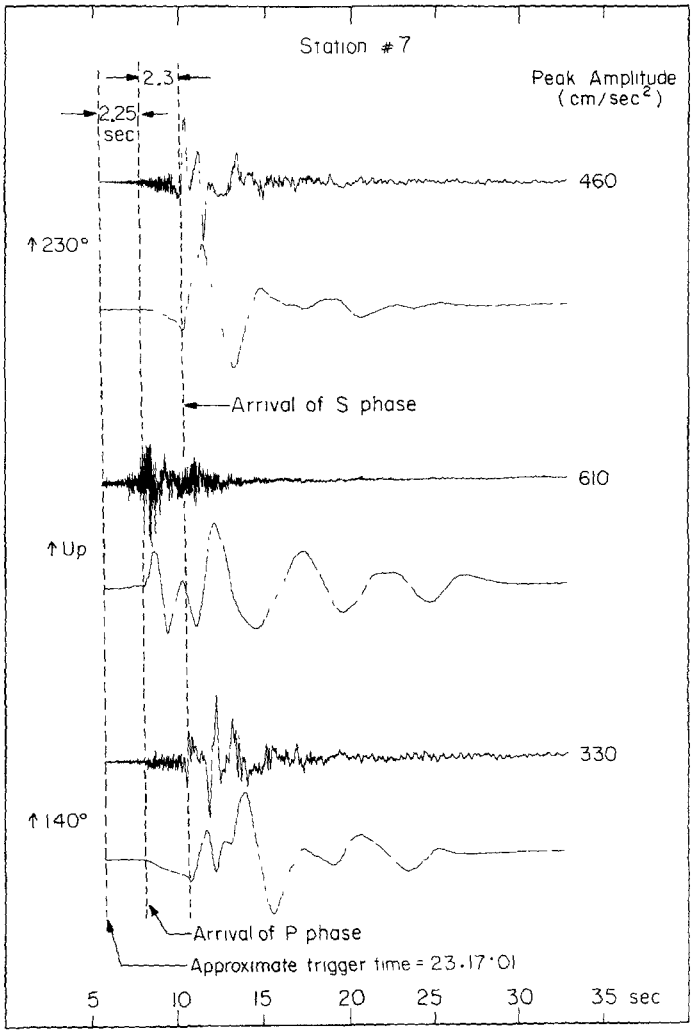

FIG. 5 Detail of array station (EL7, Imperial Valley College) record. The *first trace* is the corrected acceleration. The *second trace* is the ground motion as recorded by a damped harmonic oscillator with a free period of 5 sec and 0.7 of critical damping.

function of distance from the closest section of the trace of the Imperial fault. The first 10 sec of each record is dominated by body waves (*P* and *SV*). The waveforms spread out in time by only a small amount in moving from the trace of the Imperial fault out to a distance of 9 km. The limited dispersion indicates that the major portion of faulting occurred deep, perhaps below 5 km. Although variable in thickness, the top 5 km of the Imperial Valley appears to be sediments, possessing

a strong velocity gradient. The basement below 5 km has a relatively constant velocity down to about 12 km (Fuis *et al.*, 1981). The change in seismic velocities at 5 km is undoubtedly correlated with a change in the way accumulated strain is released. This point will be discussed in a later section in the context of the preferred fault model.

Figure 5 takes a closer look at the strong motion from one particular array station, 7. Station 7 is about 1 km from the trace of the Imperial fault and is representative of the other array stations. The *first trace* in Figure 5 is the acceleration, corrected for the response of the instrument. The *second trace* is the ground motion viewed through an alternate instrument. The alternate instrument record is obtained by first deconvolving the response of the recording instrument from the acceleration and then convolving with the response of another single-degree-of-freedom, simple, damped, harmonic oscillator. The free period of 5 sec and faction of critical damping of 0.7 of the new instrument are chosen to yield records at displacement periods.

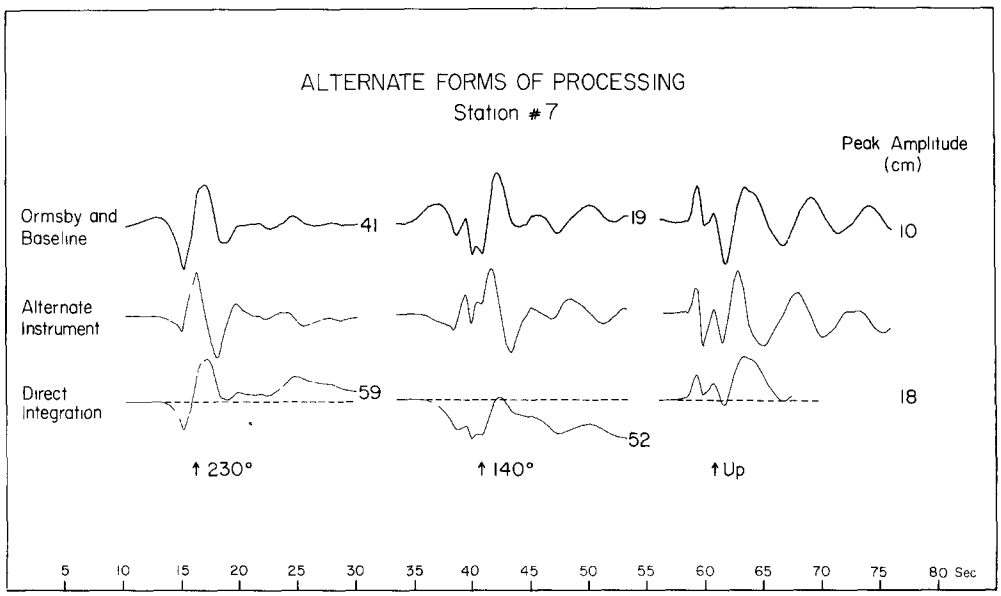

FIG. 6. Comparison of displacements for array station 7 (EL7) obtained from the accelerograms by three different processing techniques

The advantage of this form of processing over the standard parabolic baseline, Ormsby filtering is that noncausal first motions are eliminated. Figure 6 compares three forms of processing: standard Ormsby; alternate instrument; and direct trapezoidal rule integration of the acceleration. Note the noncausal first motions with the standard processing. It should also be noted that direct integration works well for this record, but is not useful for records with a greater amount of long-period drift. In such cases, a baseline correction is necessary.

Station 7 clearly triggered on low-amplitude accelerations that have very little corresponding longer period energy (Figure 5). These low amplitudes last for about 2 sec, at which point there is a major arrival on the vertical component. This arrival is characterized by a pulse-like vertical displacement and near-field *P*-type long-period displacements on the horizontal components. The waveforms in Figure 5 suggest that this arrival is a *P* wave from a later and larger break. The location of this break may not be near the hypocenter, although at this point in the analysis,

the location is indeterminate. However, it is possible to measure S-P times from the array station records as is done in Figure 5 for station 7. The results are given in Table 1. The times in Table 1 are relative to the trigger time of each instrument and have been taken from records processed similarly to those in Figure 5. The average S-P time is about 2.3 sec with no systematic increase for stations further from the fault. These results suggest a source significantly to the south of the array stations.

The salient features which have been deduced from a qualitative investigation of the strong-motion data are summarized below.

1. The overall *SH* waveform pattern at the array stations suggests that the rupture occurred to first order as a simple Haskell fault.
2. Asymmetry with respect to the Imperial fault of *SH* amplitudes and the large *P*-wave amplitudes along the strike of the Imperial fault imply complexities in faulting not explained by a simple planar Haskell model.
3. Coherence of vertical velocities and apparent lack of strong surface waves implies that most of the faulting occurred deep (possibly below 5 km).
4. The array stations triggered on low-amplitude accelerations followed about 2 sec later by a much larger amplitude impulsive arrival possibly originating from a region of greater slip north of the hypocenter, but south of the array stations.

TABLE 1

TIMES AT THE EL CENTRO ARRAY STATIONS

Station	*P* (Vertical)	*SH* (Horizontal)	$t_{(S-P)}$
7	2.27	4.55	2.28
6	1 36	3.64	2.28
8	2.55	5.18	2 63
5	2.18	5.09	2.91
DIF	2.55	4.91	2.36
4	2.45	4.73	2.28
3	4.18	6.18	2.00

DESCRIPTION OF FINITE-FAULT MODELING TECHNIQUE

In this section, we digress briefly from our analysis of the strong-motion records to explain the modeling technique employed in the following section. The method is the same as that used by Heaton and Helmberger (1979) in their study of the 1971 San Fernando earthquake. A finite fault is modeled by summing the contributions of a regular gridwork of point shear dislocations,

$$\underline{U}(t) = \sum_{j=1}^{n} \sum_{k=1}^{n} m_{jk}\, \underline{Y}_{jk}(t) * \dot{D}(t).$$

Here $\underline{U}(t)$ is the displacement at a station, j is the jth source along the fault strike, k is the kth source down the fault dip, m_{jk} is the moment and $\underline{Y}_{jk}(t)$ is the step function response of the j, kth source, and $\dot{D}(t)$ is the derivative of the time history of slip on the fault.

The point shear dislocation responses, $\underline{Y}_{jk}(t)$, were first computed using a single-layer-over-a-half-space structure, the solid curves in Figure 7. The *top layer* is intended to represent 5 km of sediments. This structure was chosen since the required Green's functions could be computed simply and inexpensively using generalized ray theory (Helmberger and Harkrider, 1978; Heaton, 1978). However,

after computing several finite-fault synthetics, it became clear that this simple structure was inadequate to explain the observations. The refraction work reported by Fuis *et al.* (1981) shows that the upper 5 km of the Imperial Valley has a pronounced velocity gradient. This gradient is probably due to the lithification of sediments and has the effect of greatly steepening the angle of incidence at the free surface. Although a velocity gradient may be approximated using many layers, the computation of Green's functions using generalized ray theory becomes quite tedious and expensive. The second velocity structure considered includes this velocity gradient and is shown in Figure 7 by the dashed curves. The *P*-wave velocities are based closely on the refraction results of Fuis *et al.* (1981). The *S*-wave velocities are obtained by assuming a Poisson solid ($\alpha = \beta\sqrt{3}$) below a depth of 5 km and varying smoothly to $b = a/2.37$ at the surface (R. Archuleta and P. Spudich, personal communication, 1981). Green's functions for this gradient structure are computed using the discrete wavenumber/finite element program (DWFE) of Olson (1978) which is similar to the finite-difference method of Alekseev and Mikhailenko

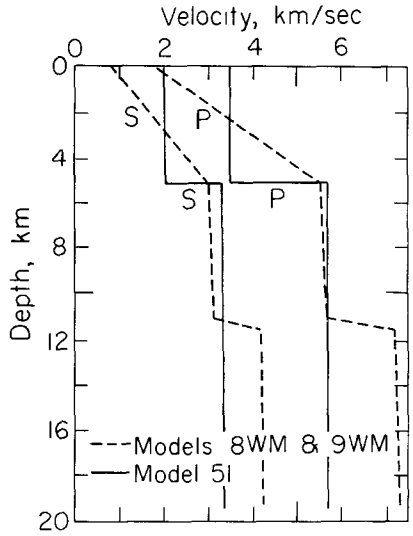

FIG 7. Two *P* and *S* velocity models for the Imperial Valley considered in this study. The gradient model is based on recent refraction profiles (Fuis *et al.*, 1981).

(1979, 1980). In the next section, we compare finite-fault synthetics for the layer-over-a-half-space structure with the Fuis *et al.* velocity gradient structure.

Examples of the functions $\int \underline{Y}_{jk}(t)\, dt$ are shown in Figures 8 and 9 for the layer-over-a-half-space structure using generalized rays. The 230° component is shown at 5° off the strike of a vertical strike-slip fault. The motion is primarily near-field *P* and *SH*. The full Cagniard solution is used for sources at small ranges where it is important to accurately compute near-field terms and static effects. At larger ranges, an asymptotic form of the solution can be used without introducing significant error. For the layer-over-a-half-space structure, it was found that accurate computation of near-field waveforms requires the full Cagniard solution for point sources at ranges $r \leqq 3$ km and angles $x \geqq 45°$, where x arctan (d/r), d being the source depth. The generalized ray paths considered are shown in the *upper right-hand corner* of Figures 8 and 9. The discrete wavenumber/finite element method computes the total wave field up to a specified frequency. There is no consideration

of rays. Both near- and far-field terms are included with this method, and the solutions are accurate in frequency content from 0 Hz. Examples of the functions $\underline{Y}_{jk}$ for the velocity gradient structure in Figure 7 computed with the discrete wavenumber-finite element method are shown in Figure 10. The Green's functions in Figure 10 have been computed to a frequency of 2 Hz, which is sufficient for modeling ground displacement. The 230°, 140°, and vertical components of displacement are shown at 5° off the strike of a vertical strike-slip fault. Some of the waveforms in Figure 10 show high-frequency oscillations which are a product of

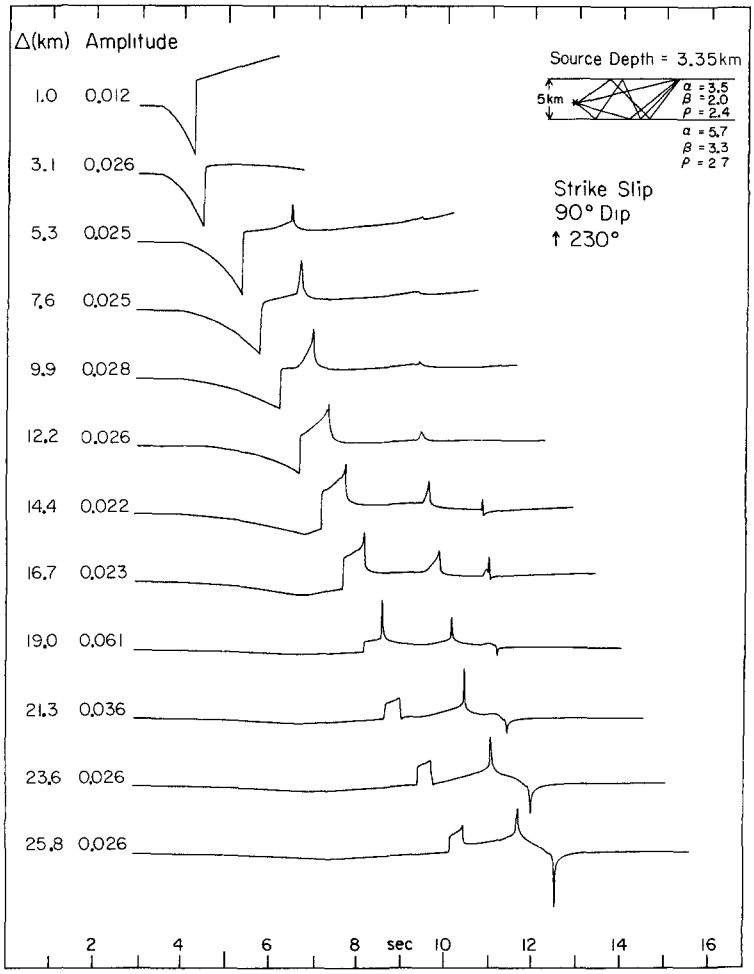

FIG. 8. Point source responses for a ramp dislocation using generalized rays for a strike-slip source within the top layer of the two-layer velocity structure in Figure 7

terminating the calculation at 2 Hz. These oscillations do not affect our results since they have random arrival times and are smoothed out in the process of forming a finite fault.

Whether the $\underline{Y}_{jk}$ functions are calculated using the generalized ray method or the discrete wavenumber/finite element method, the response of a finite fault is constructed in the same manner. A master set of Green's functions is computed for a sufficient number of ranges and depths (many more than are shown in Figures 8 to 10) such that spatially adjacent Green's functions do not vary greatly in wave shape.

Then, for a given station location and fault geometry, the required Green's functions are interpolated from the master set to uniformly cover the fault plane. The interpolation is accomplished by lining up adjacent records on the *S*-wave arrival time and using a simple liner interpolation scheme (Hartzell *et al.*, 1978; Heaton and Helmberger, 1979). The gridwork spacing is continually reduced with more and more interpolated point sources until there is no further change in the sum, $U(t)$. For the displacement synthetics in this study, the final interpolated point source spacing used is no greater than 0.5 km both along the strike and down the dip of the fault.

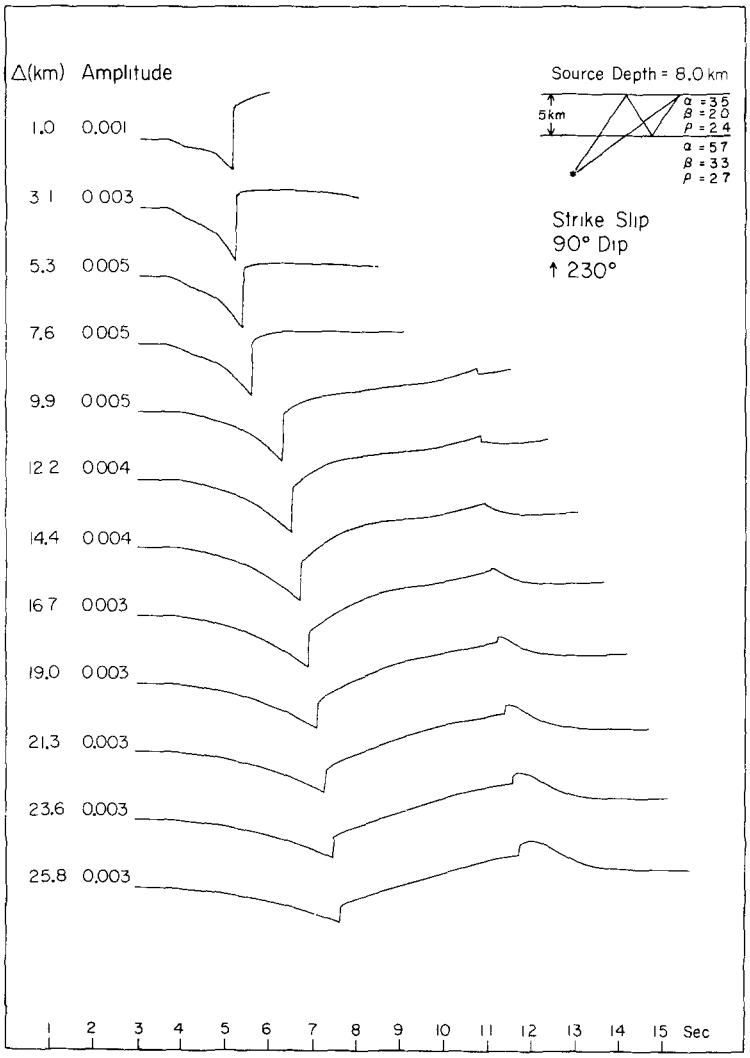

FIG. 9. Point source responses for a ramp dislocation using generalized rays for a strike-slip source below the top layer of the two-layer velocity structure in Figure 7.

FAULT MODELS

This section presents several finite-fault models and discusses the synthetics obtained by the techniques outlined in the previous section. In the accompanying figures, generalized ray synthetics are labeled GR and discrete wavenumber/finite element synthetics are labeled DWFE.

Uniform rupture model. The simplest and logically the first finite-fault model that should be investigated is a uniform rectangular fault. In this model, each of the weights on the fault plane, m_{jk}, is set equal to one. Thus, the moment contribution from each point on the fault is the same. Figure 11 compares synthetics for this model with the observed displacements for the three stations EL7 (El Centro array station 7), DIF (El Centro differential array), and BOC (Bonds Corner). (See Figure 1 for station locations.) The epicenter is 32.63°N, 115.33°W (about 5 km south of

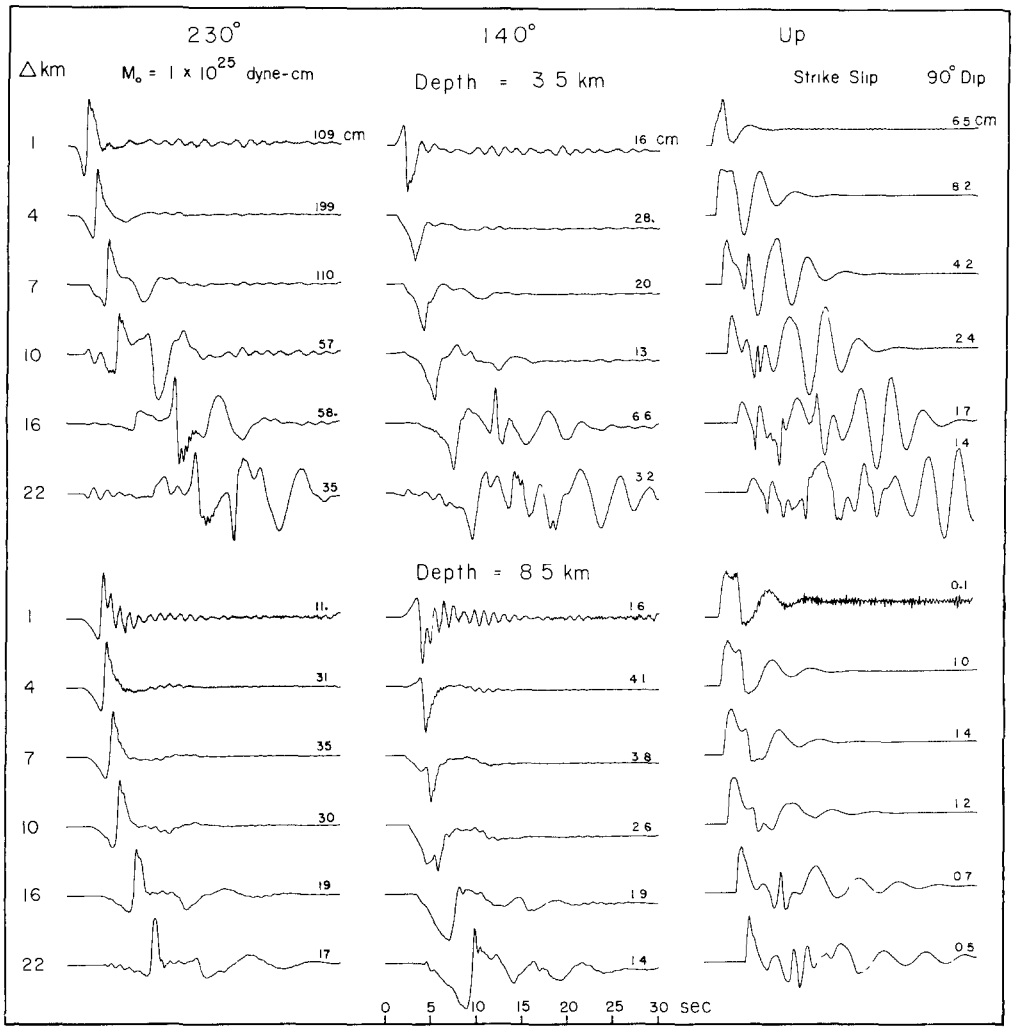

FIG. 10. Point source responses for a step dislocation using discrete wavenumber/finite elements for a strike-slip source at two different depths within the velocity gradient structure in Figure 7.

the international border) with a hypocenter at a depth of 10.5 km. The rupture is unilateral to the north with a constant velocity of 2.7 km/sec or about 0.9 the shear-wave velocity of the basement material. A circular rupture front advances from the hypocenter until it fills a rectangular region 32 km long and 10.5 km wide. The mechanism is strike slip with 90° dip. The strike is 143° clockwise from north (the average trend of the surface trace of the southern half of the Imperial fault). $\dot{D}(t)$ is assumed to be constant over the fault plane and approximated by a triangle with a 1-sec duration.

Figure 11 shows synthetics for two different velocity structures; generalized ray solution for the layer-over-a-half-space model, labeled GR, and discrete wavenumber/finite element solution for the velocity gradient model, labeled DWFE. For stations near the fault trace, like EL7, the vertical synthetics for both velocity structures are dominated by the *P* wave from the section of the fault lying at 45° to the station (*P*-wave radiation pattern maximum). The 230° component is approximately transverse to the fault and situated at an *SH* radiation pattern maximum for most of the fault plane. *SH* waves originating from the fault plane between the hypocenter and the station pile up on one another and interfere constructively in a directivity effect. After the rupture passes the station, the wave fronts are defocused, producing dispersed, long-period wave trains of much lower amplitude. Therefore,

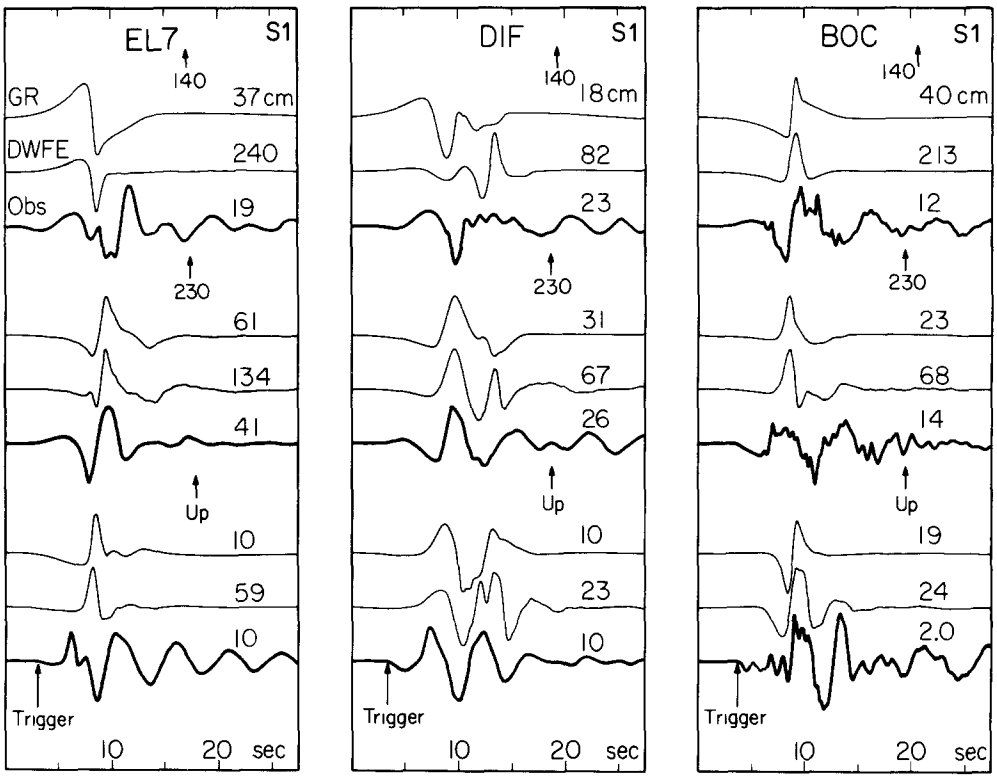

FIG. 11 Comparison of observed displacements and synthetics for a uniform rectangular fault model assuming a moment of 5.0×10^{25} dyne-cm. GR, generalized ray synthetics for two-layer velocity structure in Figure 7; DWFE, discrete wavenumber/finite element synthetics for velocity gradient structure in Figure 7

the *P*-wave pulses on the vertical components are narrow because they come from a very limited area of the fault plane, and the *SH* waveforms are relatively narrow and simple in form because of directivity. These considerations also explain the small *S-P* time of only about 1 sec for the EL7 synthetics. The larger *S-P* time of about 2.3 sec for the data indicates complexity not explained by a uniform rupture model.

Consider now station BOC. Although BOC lies off the fault trace, it also experiences a directivity effect resulting in impulsive waveforms for both velocity models. In the case of BOC, it is a vertical directivity. There is constructive addition for *P* and *S* waves that originate between the hypocenter and the surface. This vertical

directivity may be partly responsible for the large accelerations recorded at BOC (770 cm/sec^2 on 230° component). However, again we note that the simple, smooth rupture model does not yield the complexities in the data. For both EL7 and BOC, the synthetic waveforms (but not amplitudes) for the two velocity models are similar. For station DIF, which is further from the fault and not subject to strong directivity, the differences between the two velocity models are more apparent. The layer-over-a-half-space structure is still dominated by body waves, whereas the velocity gradient structure has a well-developed, later arriving surface-wave. The surface waves are, however, significantly stronger than in the data, indicating as we concluded earlier that an important percentage of the faulting occurred deep.

The amplitudes in Figure 11 are based on a moment of 5.0×10^{25} dyne-cm. The velocity gradient structure yields *SH* amplitudes about a factor of 2 larger than those for the layer-over-a-half-space structure. Since the angle of incidence at the free surface does not affect the amplitude of *SH* waves, the above observation is easily traced to the difference in near-surface rigidities. The steeper angle of incidence in the velocity gradient structure tends to polarize the *P* wave onto the vertical component and the *SV* wave onto the 140° component. Thus, the vertical and 140° components are amplified by both the lower rigidity and the steeper incident angle. Finally, the uniform rupture model produces amplitudes which are too large (for a moment of 5.0×10^{25} dyne-cm), again indicating that more of the faulting must have occurred at depth.

Layer-over-a-half-space fault model. It is instructive to discuss one finite-fault model which uses the layer-over-a-half-space velocity structure despite this model's shortcomings, since by investigating other velocity models, we obtain a better understanding of the effects that a particular structure has on strong ground motion. Figure 12 shows contoured dislocation in meters on the Imperial fault plane assuming a moment of 5.0×10^{25} dyne-cm for three different models. Model 51 was obtained using the layer-over-a-half-space structure. Models 8 and 9 WM were obtained using the velocity gradient structure and are discussed later. The dip of the fault plane for model 51 is 90°, rake 180° (right-lateral strike-slip), epicenter 32.63°N, 115.33°W, hypocenter at a depth of 10.5 km, and unilateral rupture to the north at 3.0 km/sec. Before switching to the velocity gradient structure, model 51 was considered the best-fitting solution to a subset of five of the strong-motion stations shown in Figure 13.

Although the synthetics in Figure 13 do not fit the observed displacements particularly well, model 51 still has several of the general characteristics of the presently preferred model, 9 WM. Most of the faulting occurs in the basement material below the sediments; there is an area of larger dislocations south of the El Centro array but north of the border, and the distribution of surface offsets is generally consistent with the observations. The region of larger dislocations below a depth of 5 km is included in model 51 to produce the previously noted arrival at the array stations having an *S-P* time of about 2.3 sec (see Table 1). But since the layer-over-a-half-space structure gives shorter *S-P* travel times for a given range compared with the velocity gradient structure, this region of greater slip is misplaced in model 51. Using the velocity gradient structure, the area of larger dislocations shifts to the north, to under Interstate 8, leaving behind a broader region of relatively large fault offsets (i.e., model 9 WM). The strike of the fault is not constant in model 51. To model the previously mentioned large *P*-wave amplitudes at array stations lying near the fault strike, the region of larger dislocations in model 51 is given a strike of 155° (see Figure 12). The remainder of the fault plane has a strike of 143°, consistent with the trend of the surface trace.

Two synthetics are shown in Figure 13 for station BOC, one with and one without a foreshock. Station BOC seems to be modeled better with the addition of a magnitude 5 foreshock at the hypocenter of the main shock and preceding the main rupture by 2.0 sec. This conclusion is also supported by the models run with a velocity gradient. However, the term foreshock is used rather loosely here. The actual faulting process may only involve a variable rupture velocity; initially high, then low, then high again for the remainder of the fault plane. The vertical components at stations DIF, EL7, and MEL for model 51 have large SV components (labeled in Figure 13). This SV phase is not seen in the data. Using the Fuis *et al.* gradient structure, the SV phase is shifted off the vertical component and onto the

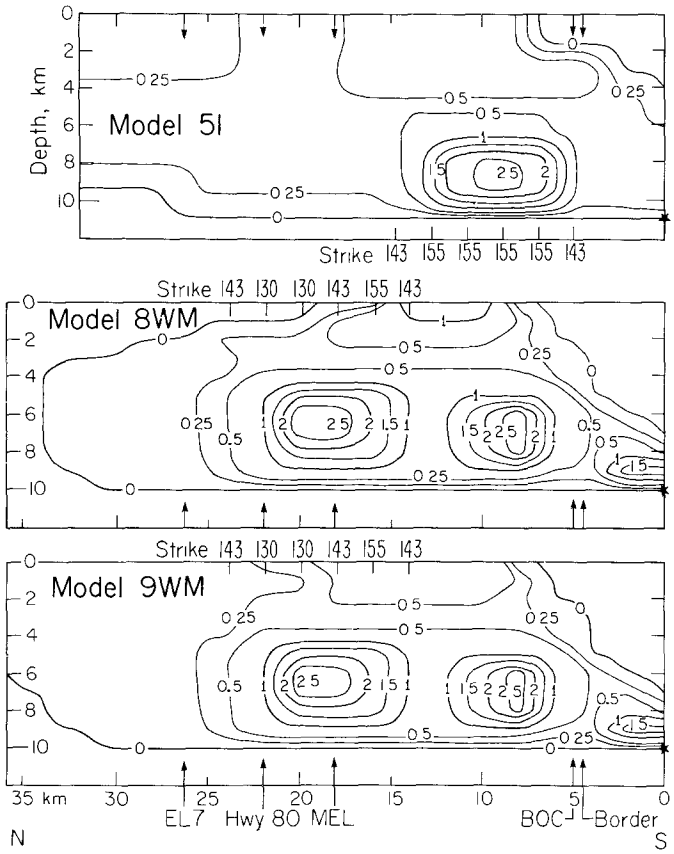

FIG. 12 Contoured dislocation in meters on the Imperial fault for three different fault models. Model 51 was derived using the two-layer velocity structure and models 8 and 9 WM were devised using the velocity gradient structure in Figure 7 9 WM is the preferred fault model.

140° component. The synthetic labeled DWFE in Figure 13 for station EL7 uses the gradient structure. However, there is still a large phase, labeled P_b, on the vertical component. P_b is a P wave originating from much closer to the station where the P-wave radiation pattern is a maximum. Obviously model 51 still does not achieve the correct P-wave radiation distribution.

Velocity gradient fault model. The preceding discussions were included in part to motivate the reasoning which led to the presently preferred fault model, model 9 WM in Figure 12. The model parameters are listed in Table 2. Synthetics for model 9 WM are compared with the observed displacements in Figure 14, a and b, where again we assume a triangular shaped $D(t)$ with a 1-sec duration. In general, the

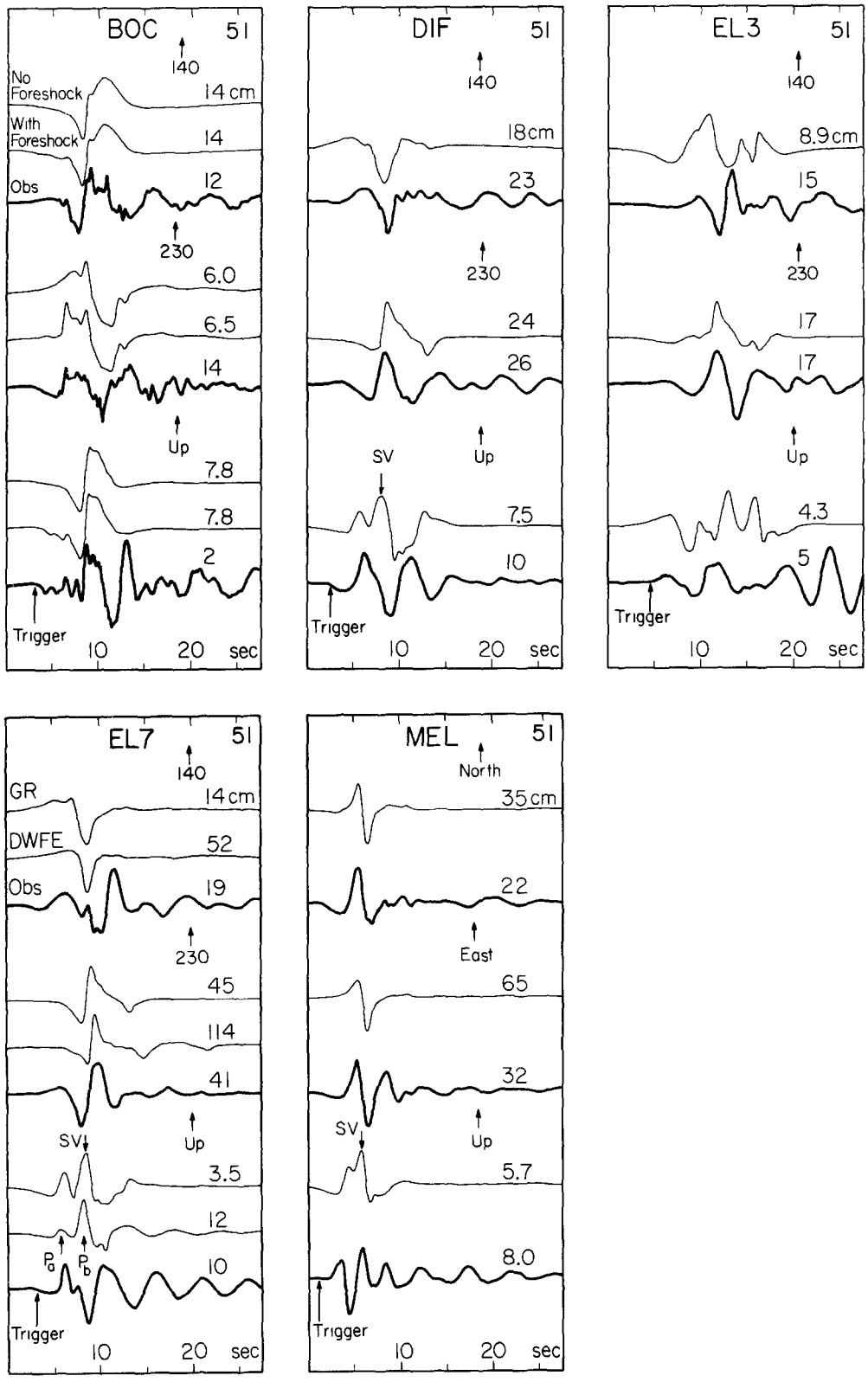

FIG. 13. Comparison of observed displacements and synthetics for fault model 51 All are generalized ray synthetics for the two-layer velocity structure in Figure 7 except the one labeled DWFE for station EL7. The two synthetics for station BOC (Bonds Corner) show the effect of adding a magnitude 5 foreshock 2.0 sec before the main rupture.

waveforms and amplitudes are fit quite well. However, the predicted horizontal ground motion for the two stations very near the fault strike (EL7 and MEL) is too large. This discrepancy may be due to scattering and rupture incoherencies that are not in our model. The fault plane has a strike of 143° except for the region under station MEL, where the fault strike is varied to produce an "S" shape or corrugated pattern when viewed from above (see Figure 12). This complexity has been added to produce the *P* waveform at EL7 and is not strongly required or excluded by the other stations. The vertical synthetic for MEL is missing a leading up and down swing suggesting that a similar wiggle in the fault plane exists for the region of larger dislocations just north of the border. In general, stations like EL7 and MEL are not particularly useful in recovering the distribution of slip. They are too close to the fault and, therefore, too sensitive to subtle changes in fault parameters. BOC is a much more useful station. A very diagnostic array would have stations parallel to the fault at about 5 km from the surface trace. The localized source south of the border and just above the hypocenter in model 9 WM (see Figure 12) is a foreshock preceding the main rupture by 2.0 sec. The moment of the foreshock is 1.0×10^{24} dyne-cm ($M_L = 5.3$). As mentioned earlier, this may not be a foreshock in the usual sense of the word. Of the stations modeled, BOC is the only one requiring the foreshock since the foreshock's displacements are very small at the other stations. However, the 2.25 sec of low level accelerations following triggering of the array stations (see Figure 5) may be due partly to this foreshock.

TABLE 2

MODEL PARAMETERS FOR FAULT MODEL 9 WM

Strike	143° clockwise from north, with "corrugations"
Dip	90°
Rake	180° (right-lateral, strike-slip)
Moment	5.0×10^{25} dyne-cm
Rupture Velocity	2.5 km/sec, unilateral to the north
Epicenter	32.63°N, 115.33°W
Depth	10.5 km

One question of interest is how much of the observed surface slip occurred coseismically and how much occurred as sympathetic creep? Models 9 and 8 WM are very similar except for the amount of slip allowed in the sediments north of Interstate 8 (or station MEL). These two models produce very nearly the same displacements at all 12 stations modeled except for the two closest, EL7 and MEL. Two vertical synthetics are shown in Figure 14 for station EL7, one for model 9 WM and the other for 8 WM. The differences are not large. The data are insensitive to the exact distribution of shallow faulting as long as it is small. The data are compatible with all of the shallow surface faulting north of MEL occurring as creep. The data is also rather insensitive to the amount of deep faulting north of the El Centro array. Because the rupture on this section of the fault plane propagates away from most of the stations, the resulting amplitudes are low. However, the amount of faulting north of the array must be small compared to the amount south of the array.

The synthetics in Figure 14 are for a rupture velocity of 2.5 km/sec or about 0.8 of the basement shear-wave velocity. However, the synthetics do not change a great deal when a rupture velocity of 2.7 km/sec (0.9 of the basement shear-wave velocity) is used. So we are limited in the resolution of the average rupture velocity to 2.5 to 2.7 km/sec. Although our preferred model uses a unilateral rupture to the north, the data we have modeled would also allow a small amount of rupture to the south.

Finally, we note that most of the vertical synthetics in Figure 14, a and b, appear as if they would match the observations better if they were shifted to the left a small amount. This discrepancy in phasing is attributed to an incorrect Poisson ratio in

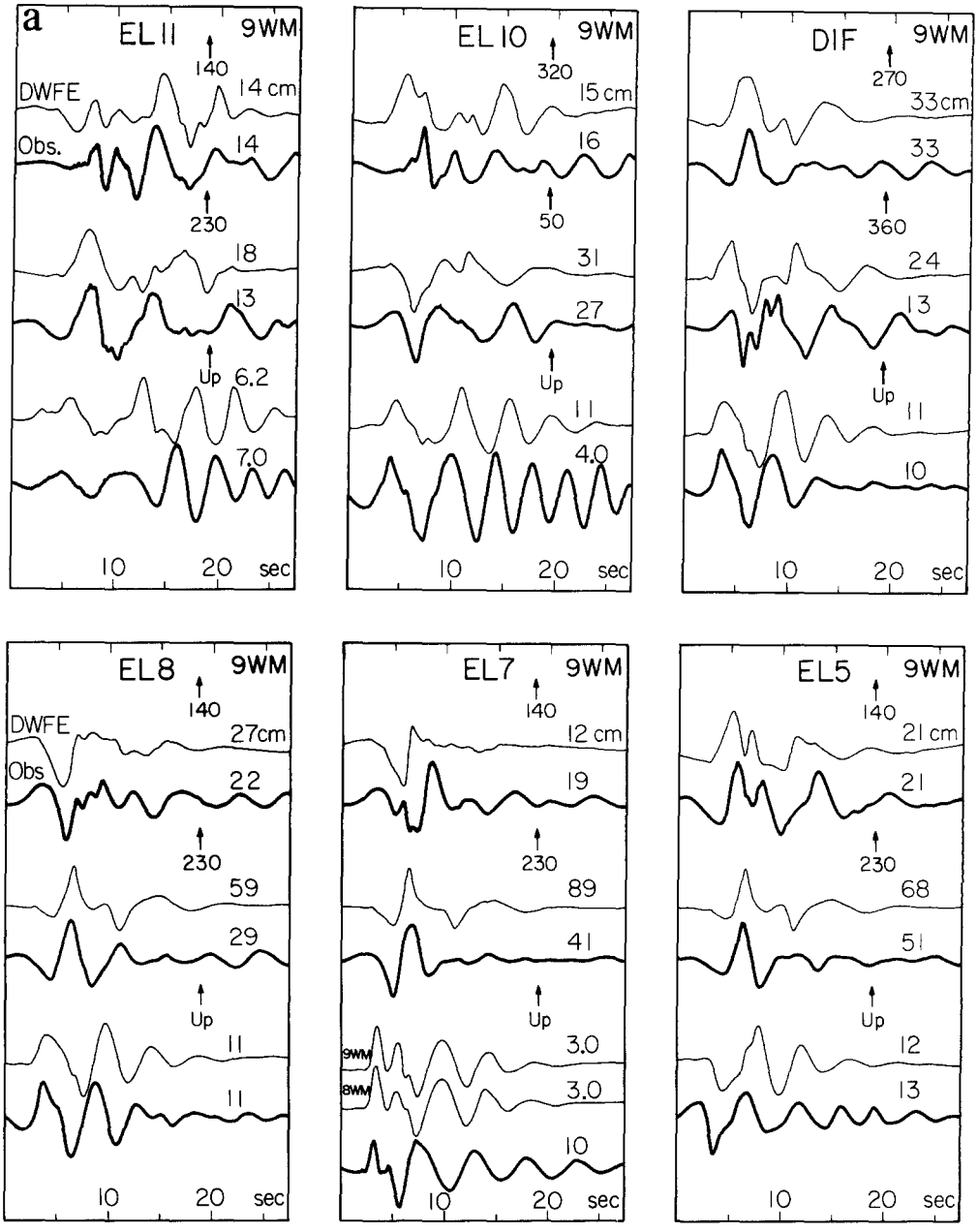

FIG. 14. Comparison of observed displacements and synthetics for the preferred fault model, 9 WM All are discrete wavenumber/finite element synthetics for the velocity gradient structure in Figure 7. The hypocenter for each model is indicated by *. (EL3 to EL5, EL7, EL8, EL10, and EL11 are El Centro array stations, DIF, El Centro differential array, MEL, Meloland Overpass; BOC, Bonds Corner; CAL, Calexico; HOL, Holtville).

the sediments, although this interpretation is subject to considerable uncertainty. Therefore, at this stage of modeling, we have placed a greater emphasis on fitting the *SH* and *P*-wave portions of these motions. We adopted this position because of

the strong interference between P and SV arrivals starting at the SV onset. The time separation between these arrivals is controlled by the rupture process and crustal structure. The latter structure is not well known since most refraction studies

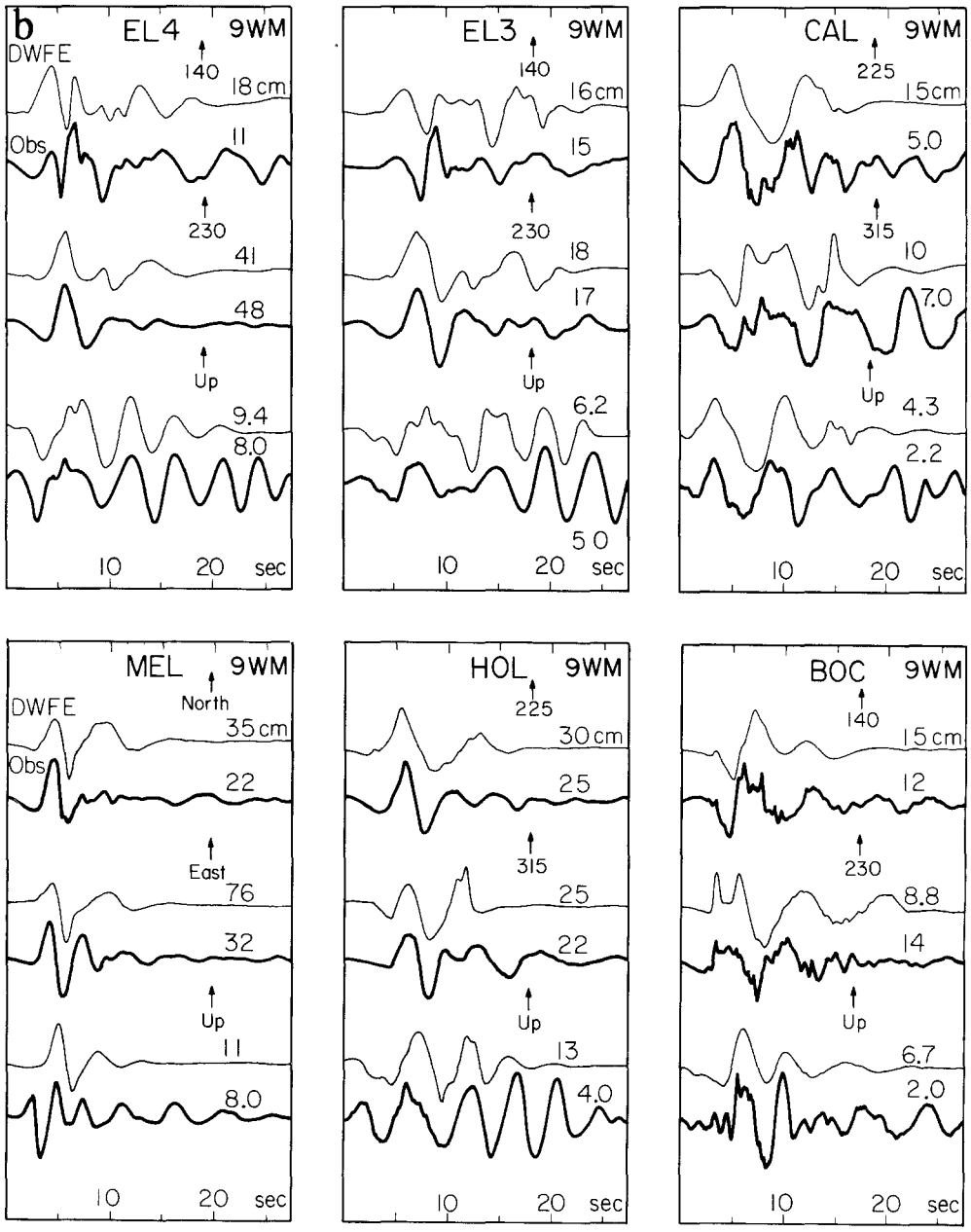

FIG. 14. Continued.

are done with P waves. A better appreciation of the importance of shallow velocity structure on the various components of motion awaits the many aftershock studies now in progress such as Liu and Helmberger (1980).

Discussion

An important question to be asked of any fault model derived from near-field strong-motion records is how well does the moment compare with the teleseismic body-wave moment? The teleseismic body-wave moment is certainly an important datum, and the moment obtained from a near-field study should not be greatly different. Short of modeling the teleseismic body waves for the Imperial Valley earthquake, we can make a simple comparison to answer the above question. The 1968 Borrego Mountain earthquake has a similar mechanism and location to the

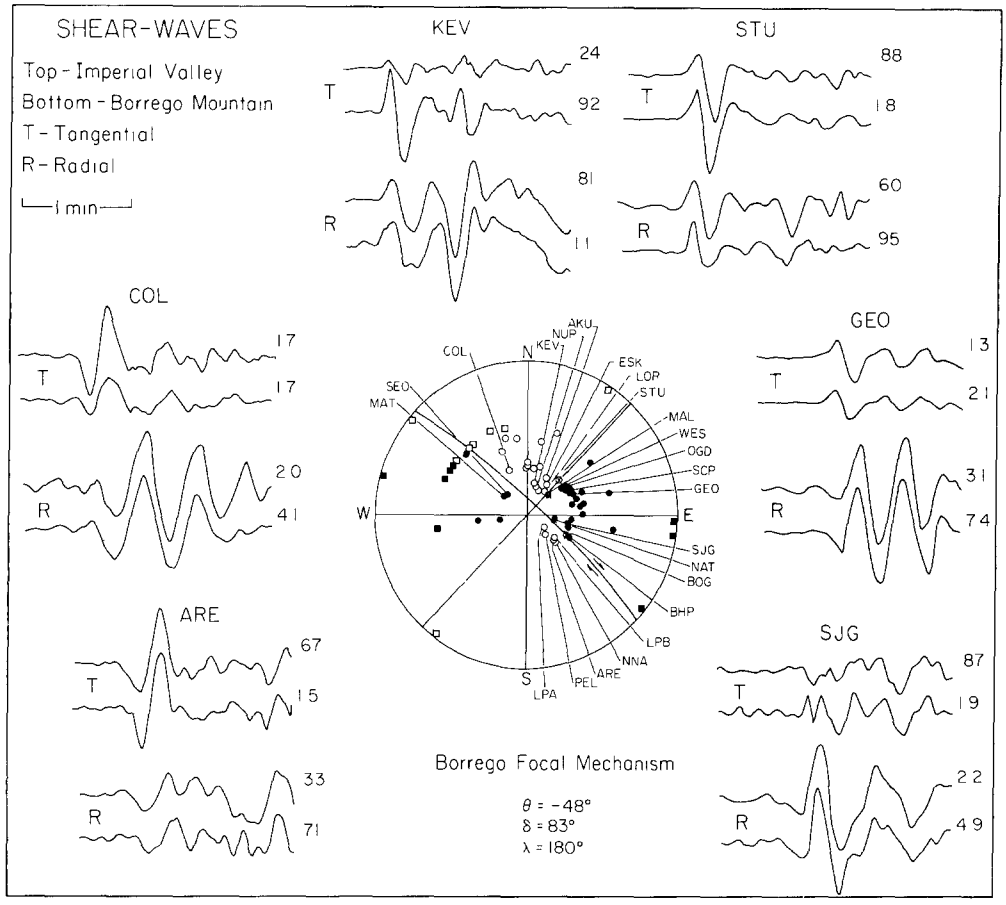

FIG. 15 Comparison of rotated teleseismic shear waves for the Borrego Mountain (*Bull Seism Soc Am.* $M_0 = 1.1 \times 10^{26}$ dyne-cm) and Imperial Valley ($M_0 = 5.0 \times {}^{25}$ dyne-cm) earthquakes. Amplitudes are in units of 10^{-3} cm

1979 Imperial Valley earthquake. Figure 15 compares rotated *S* waves (radial and transverse components) from selected WWSSN stations for these two events. The waveforms are amazingly similar at a wide range of azimuths except for amplitude differences. The moment of the Borrego Mountain earthquake from a study of teleseismic body waves is 1.12×10^{26} dyne-cm (Burdick and Mellman, 1976). From Figure 15, it is clear when we neglect nodal components that the Imperial Valley earthquake runs consistently a factor of 2 smaller than the Borrego Mountain earthquake. The moment of 5.0×10^{25} dyne-cm for Imperial Valley determined in

this study is very consistent with the above data. The fact that *SV* (radial components) is also proportionately smaller for Imperial Valley than for Borrego Mountain indicates that there is not significant normal faulting associated with the Imperial Valley earthquake.

In model 9 WM major faulting initiates at the surface and at depth just north of the border. This characteristic of the model is consistent with the observed surface faulting. Figure 16 compares the measured surface offsets for the 1979 and 1940 Imperial Valley earthquakes. The 1979 curve is based on work by Sharp *et al.* (1981). The 1979 offsets are zero in the epicentral region and remain so until about 5 km north of the border. At this point, there is an almost step-like discontinuity, with the offsets rising to their maximum values of 60 to 70 cm. The 1940 curve is based on unpublished field notes of J. P. Buwalda and is less accurate than the 1979 curve. The 1940 event apparently ruptured primarily to the south from an epicenter about 10 km north of the border (see Figure 1). However, there is a prominent increase in the surface offsets for the 1940 earthquake in the same area as the abrupt decrease in offsets for the 1979 earthquake. Both of these rapid changes in surface offsets lie above the region of large dislocations just north of the border in model 9

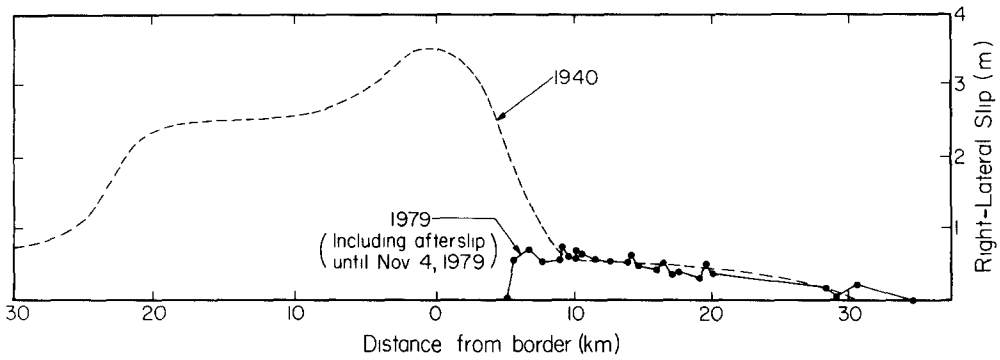

FIG. 16 Comparison of the measured surface offsets for the 1940 and 1970 Imperial Valley earthquakes

WM. Hartzell (1978) modeled the El Centro displacement record for the 1940 Imperial Valley earthquake by summing aftershock records. In that study, the aftershock records are treated as empirical Green's functions. It was found that a reasonable fit could be obtained to the El Centro record if the earthquake is treated as four separate events. Three of these events and the aftershock used to represent their ground motions are situated in the same general region as the localized large dislocation source 3 km north of the border in model 9 WM. Thus, this same region of the fault plane was apparently also important in 1940.

Figure 17 shows aftershock epicenters for the first 26 days following the 15 October 1979 earthquake (Johnson and Hutton, 1981). The vast majority of aftershocks occur at the very northern end of the observed ground breakage and extend further to the north. A clear exception to this pattern is the obvious pocket of aftershocks located north of the border but south of El Centro. The depths of several of these aftershocks were accurately determined by Peter German of the USGS at Caltech. All the events considered consistently fall at a depth of 8.5 km $\pm$ 0.5 km. Referring to model 9 WM (Figure 12), the pocket of aftershocks plots between the two maxima in dislocation in the distance range of 12 to 15 km north

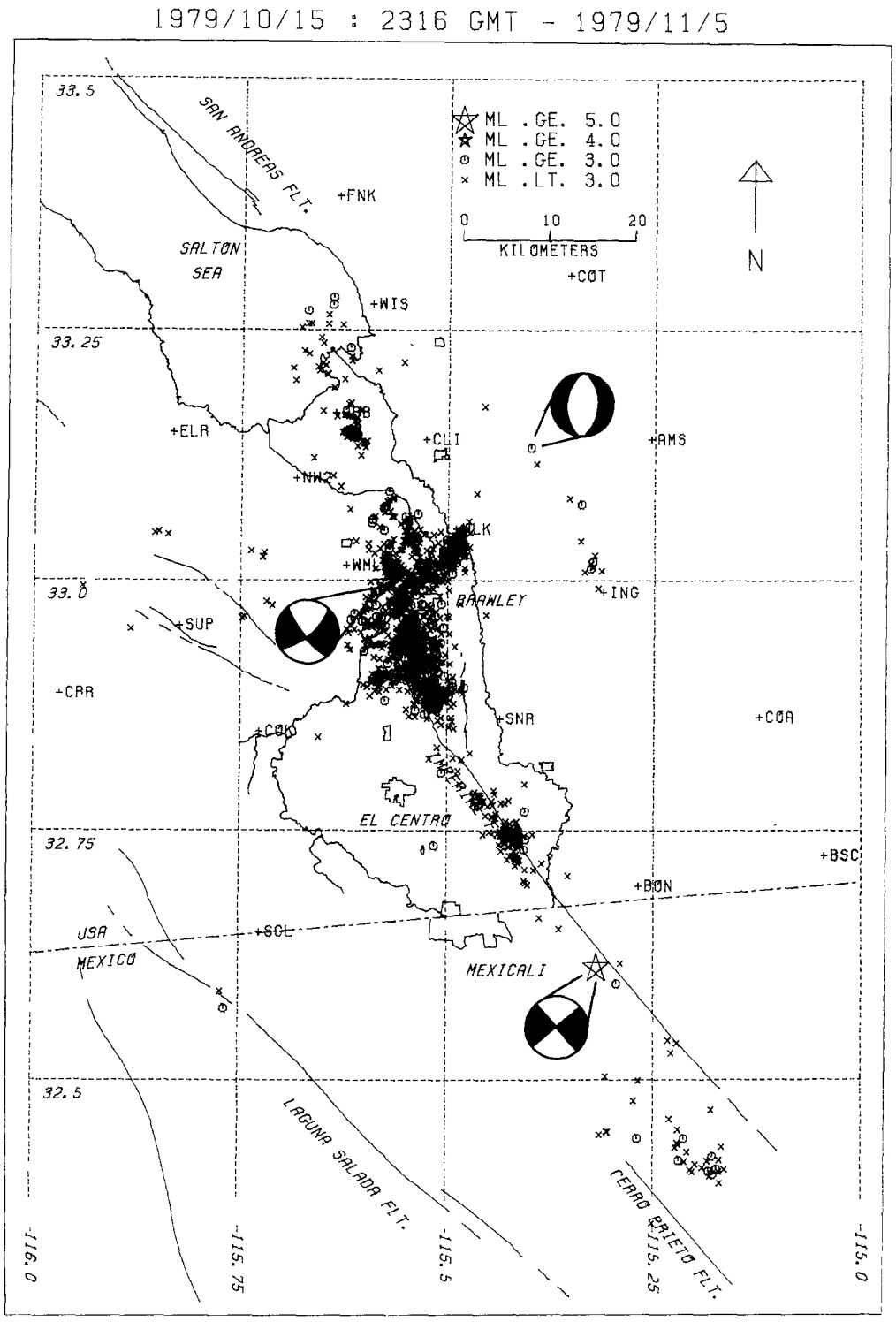

FIG 17. Aftershock epicenters for the first 26 days following the 15 October 1979 earthquake from Johnson and Hutton (1981).

of the epicenter. These aftershocks may represent a readjustment to the strain field created by the flanking larger dislocations.

The large amplitude vertical accelerations recorded at the array stations are coincident in time with pulses on the vertical displacement records. The relationship is clearly seen in Figure 5 for station EL7. The same is true for station EL6 which recorded a peak vertical acceleration of 1.7 g. In this paper, the vertical displacement pulses at the array stations are explained by the breaking of a localized source, located about 8 km to the south under station MEL. The strike of this source is also varied. However, unusually high accelerations are not observed at MEL or any of the other stations north or south of the EL Centro array. To explain this apparent contradiction, one is left with propagation and path-effect arguments. Although the faulting under MEL seems to be the source region for the seismic waves that generated the high accelerations, the high frequencies did not necessarily travel the full distance to the array stations. The high frequencies could be produced near the array stations by critical reflections within the near-surface sedimentary layers (Liu and Helmberger, 1980). Directivity is probably also a factor. The highest accelerations and narrowest displacement pulses are along the strike of the fault (stations EL6 and EL7). However, directivity in the P-wave radiation implies a very high-rupture velocity, close to the P-wave velocity. Part of the source under MEL, a localized asperity, may have broken with a high-rupture velocity. Finally, a local site amplification may also be a contributing factor. Observations of other local earthquakes at the sites of the El Centro array stations yield higher amplitudes at EL6 by about a factor of 2 to 3 (Mueller and Boore, 1981).

We may estimate the stress drop for the 1979 Imperial Valley earthquake using the expression of Knopoff (1958) for a long-shallow strike-slip fault, $\Delta\sigma = (2\mu\bar{u})/(\pi W)$. μ is the rigidity, $\bar{u}$ is the average dislocation, and W is the fault width or depth. Using $\mu = 2.5 \times 10^{11}$ dyne/cm^2, $\bar{u} = 30$ cm, and $W = 10$ km, we obtain a stress drop of 5 bars. If $\bar{u} = 50$ cm and $W = 8$ km, then $\Delta\sigma = 10$ bars. These are low estimates considering the large accelerations of over 1 g. However, the stress drop may also be estimated for the localized regions of larger dislocation in model 9 WM. In this case we use the expression for a circular fault, $\Delta\sigma = (7\pi\mu\bar{u})/(16a)$ (Eshelby, 1957; Keilis-Borok, 1959), where a is the radius. Setting $\bar{u} = 150$ cm and $a = 2.5$ km, the localized stress drop is about 200 bars. This pattern of uneven slip distribution is not unlike that obtained recently by Ebel and Helmberger (1981) for the Borrego Mountain earthquake. They find two zones of high energy release separated in time by about 2 sec with an overall duration of less than 5 sec. Teleseismic long-period body-waves cannot resolve these small details and, thus, the Borrego Mountain and Imperial Valley events have relatively simple point source SH wave shapes as displayed in Figure 15 with overall modest stress drops.

The preferred fault model, 9 WM in Figure 12, has some interesting qualities which relate to other features of faulting and mode of strain release in the Imperial Valley. Figure 18 shows well-located epicenters (horizontal error less than 2.5 km) in the Imperial Valley for the time period 1973 to 1978 (Johnson, 1979). The obvious band of seismicity extending from the southern end of the San Andreas fault to about the latitude of 32.75°N is termed the Brawley seismic zone by Johnson (1979). The overall pattern of faulting in the Imperial Valley is one of northwest-trending strike-slip faults separated by dextral offsets. Swarm activity is concentrated along these dextral offsets. Johnson (1979) has demonstrated that swarms of the northern half of the Imperial fault trend originate on a vertical plane and then migrate north or south. (Without this information, one may be inclined to misinterpret the pattern

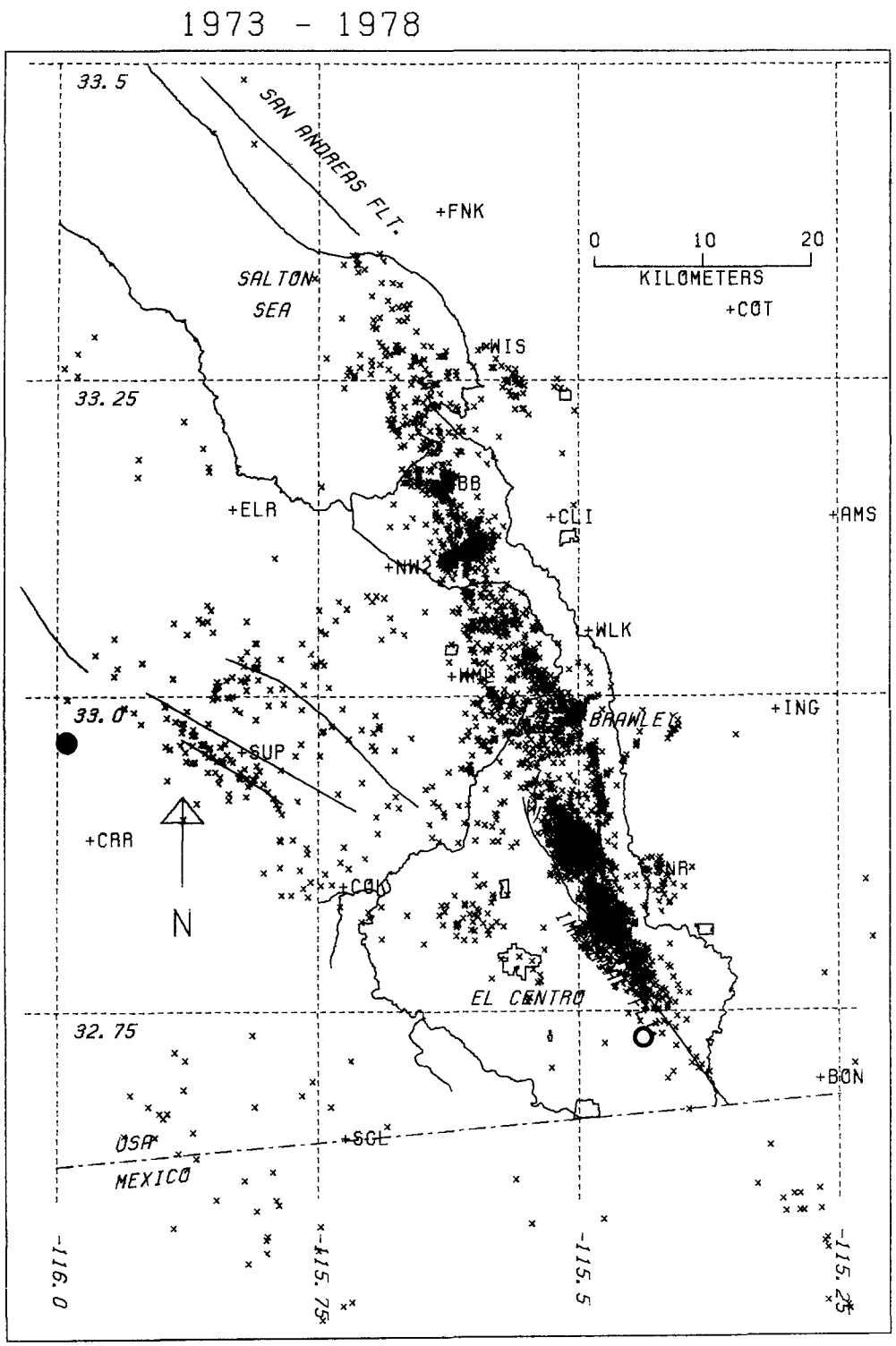

FIG. 18. Well-located epicenters (horizontal error less than 2.5 km) within the Imperial Valley for the time period 1973 to 1978 from Johnson (1979)

of seismicity as indicating a northeast dip on the Imperial fault). Johnson theorizes that this swarm activity is due to fault creep events. In contrast, the southern half of the Imperial fault is largely aseismic during the time period pictured in Figure 18. The Imperial fault is characterized by an occasional large event, such as the 1940 and 1979 earthquakes, with aseismic creep on just the northern half of the fault. Most of the dislocation in model 9 WM is concentrated on the aseismic section. The southern half of the Imperial fault apparently acts as a locked section that breaks violently. The comparison of models 9 and 8 WM showed that faulting north of the El Centro array is largely insignificant and may have occurred as creep. There are numerous observations of creep on the northern half of the Imperial fault and the Brawley fault (see Johnson,, 1979, for a summary). In particular, surface cracks reported along the Brawley fault during the 1975 swarm, which appear very similar to those following the 1979 earthquake, are attributed to aseismic creep (Sharp, 1976; Johnson and Hadley, 1976). Model 9 WM is, therefore, consistent with the observed seismicity pattern and our best estimates of the mode of strain release in the Imperial Valley.

Acknowledgments

The authors benefited greatly from discussions with Tom Heaton. The finite-fault, Green's function summation program used was written by Tom Heaton. The authors are also grateful to Alan Olson for supplying a copy of his discrete wavenumber/finite element program (DWFE) David Harkrider assisted in programming the vertical component for DWFE Informative discussions were also had with Ralph Archuleta and Paul Spudich. The wording of the manuscript was significantly improved by Tom Hanks and an anonymous reviewer This research was supported by the Earth Sciences Section, National Science Foundation Grant PFR 7921769.

References

Alekseev, A S and B G Mikhailenko (1979) Numerical modelling of transient wave fields in seismology and seismic prospecting (vertically-inhomogeneous half-space and radially-inhomogeneous sphere), Siberian Branch of the Academy of Sciences of the USSR, Novosibirsk

Alekseev, A S and B G Mikhailenko (1980) Solution of dynamic problems of elastic wave propagation in inhomogeneous media by a combination of partial separation of variables and finite difference methods (submitted for publication).

Archuleta, R. J and P. Spudich (1981) A seismological analysis of the acceleration generated by the 1979 Imperial Valley, California earthquake, IASPEI meeting, London, Ontario

Brady, A. G., V. Perez, and P. N Mork (1980). The Imperial Valley earthquake, October 15, 1979, digitization and processing of accelerograph records, *U.S Geol Surv, Open-File Rept. 80-703*

Burdick, L. J and G. R. Mellman (1976) Inversion of the body waves from the Borrego Mountain earthquake to the source mechanism, *Bull. Seism. Soc. Am* **66,** 1485–1499.

Ebel, J. and D. V. Helmberger (1981). *P*-wave complexity and fault asperities the Borrego Mountain, California, earthquake of 1968, *Bull Seism. Soc Am.* **72,** 413–437.

Eshelby, J. D (1957). The determination of the elastic field of an ellipsoidal inclusion and related problems, *Proc. Roy. Soc. London, Series A* **241,** 376–396

Fuis, G S., W D. Mooney, J H. Healy, G A. McMechan, and W. J. Lutter (1981) Crustal structure of the Imperial Valley region, *U.S. Geol. Surv. Profess. Paper 1254.*

Hartzell, S (1978) Earthquake aftershocks as Green's functions, *Geophys Res. Letters* **5,** 1–4.

Hartzell, S , G. A. Frazier, and J N. Brune (1978). Earthquake modeling in a homogeneous half-space, *Bull. Seism Soc Am.* **68,** 301–316.

Heaton, T H. (1978). Generalized ray models of strong ground motion, *Ph.D. Thesis,* California Institute of Technology, Pasadena, California.

Heaton, T. H and D. V. Helmberger (1979) Generalized ray models of the San Fernando earthquake, *Bull Seism. Soc. Am* **69,** 1311–1341.

Helmberger, D. V. and D. Harkrider (1978). Modeling earthquakes with generalized ray theory, in *Modern Problems in Elastic Wave Propagation,* J. Miklowitz and J D. Achenbach, Editors, John Wiley and Sons, New York.

Johnson, C. E. (1979) I CEDAR—An approach to the computer automation of short-period local seismic networks II. Seismotectonics of the Imperial Valley of Southern California, *Ph.D. Thesis*, California Institute of Technology, Pasadena, California.

Johnson, C E and D. M. Hadley (1976) Tectonic implications of the Brawley earthquake swarm Imperial Valley, California, January, 1975, *Bull Seism Soc Am* **66,** 1133–1144

Johnson, C E. and K. Hutton (1981) Aftershocks and prior seismicity of the 1979 Imperial Valley earthquake, *U S. Geol Surv. Profess. Paper 1254*

Kanamori, H. and J Regan (1981). Long-period surface waves generated by the Imperial Valley earthquake of 1979, *U S Geol. Surv. Profess. Paper 1254*

Keilis-Borok, V. (1959) On estimation of the displacement in an earthquake source and of source dimensions, *Ann Geofis* **12,** 205–214

Knopoff, L. (1958). Energy release in earthquakes, *Geophys. J.* **1,** 44–52.

Langston, C. A. (1978). The February 9, 1971 San Fernando earthquake· a study of source finiteness in teleseismic body waves, *Bull Seism. Soc. Am.* **68,** 1–29.

Liu, H -L and D. Helmberger (1980). S83, an explanation for high frequency vertical strong motions recorded in sedimentary basins, *EOS* **61,** 1036.

Mueller, C. S. and D. M Boore (1981) Site amplification at El Centro strong motion array station #6, *Earthquake Notes* **52,** 84

Olson, A. H (1978) Synthesizing ground motion using a discrete wavenumber/finite element representation, *Trans. Am. Geophys Union* **59,** 1128.

Sharp, R. V (1976) Surface faulting in Imperial Valley during the earthquake swarms of January–February 1975, *Bull. Seism Soc Am* **66,** 1145–1154.

Sharp, R. V., *et al.* (1981). Surface faulting in central Imperial Valley, *U.S. Geol. Surv. Profess. Paper 1254*

SEISMOLOGICAL LABORATORY
CALIFORNIA INSTITUTE OF TECHNOLOGY
PASADENA, CALIFORNIA 91125

Manuscript received 24 August 1981